Optics Letters

Multiband topological states in non-Hermitian photonic crystals

JIAPEI JIANG, BEI YAN, YUCHEN PENG, JIANLAN XIE, AOQIAN SHI, AND JIANJUN LIU*

Key Laboratory for Micro/Nano Optoelectronic Devices of Ministry of Education & Hunan Provincial Key Laboratory of Low-Dimensional Structural Physics and Devices, School of Physics and Electronics, Hunan University, Changsha 410082, China
**Corresponding author: jianjun.liu@hnu.edu.cn*

Received 26 November 2021; accepted 13 December 2021; posted 15 December 2021; published 14 January 2022

Novel phenomena found in non-Hermitian systems and robust edge states have attracted much attention. When non-Hermitian parameters (gain and loss) are above a critical value, the non-Hermitian photonic crystal (PC) bandgaps close, leading to a mixture of the topological edge state (TES) and topological corner state (TCS) with the bulk state. Meanwhile, new bandgaps also open, in which new TES and TCS can appear. Thus, with appropriate non-Hermitian parameters, TES can emerge in both the original bandgaps and the newly opened bandgaps. The results described here will further enrich understanding of the topological properties of non-Hermitian systems.

https://doi.org/10.1364/OL.449733

The robust topological edge states (TESs) and topological corner states (TCSs) of topological insulators (TIs) have inspired the development of similar edge/corner states in classical systems, including photonics [1–10], acoustics [11–13], and electrics [14–17]. Parity–time (PT) symmetric systems are of interest as they exhibit many intriguing phenomena at exceptional points (EPs) [18–20], including non-reciprocal transmission [21–24], power oscillation [25,26], and laser absorption [27,28]. In recent years, research on the combination of topology and non-Hermiticity has attracted enormous attention [29–42]. It has been found that non-Hermitian parameters can lead to the breakdown of bulk–boundary correspondence [30–33], a promising direction of research for new topological invariants in non-Hermitian systems [34–38]. By increasing the gain parameter beyond the EP, a trivial band can be tuned into a non-trivial band, with topological states emerging [39,40]. Dynamically distributing the gain area can create a reconfigurable edge state [39].

By introducing gain and loss with PT symmetry, TESs and TCSs that are different from those in Hermitian topological systems can be realized. The TESs can be tuned to be either attenuating or amplifying depending on the signs of the non-Hermitian parameters [41]. A pseudo-hinge state is found in PT-symmetric photonic [5] and phononic [42] crystals. Previous works introduced small amounts of gain and loss, as it is thought that non-trivial bandgaps in PT-symmetric systems usually become degenerate when gain and loss increase beyond the PT breaking threshold [40], causing the disappearance of TESs and TCSs. However, a PT-symmetric system will also open up new bandgaps at other frequencies as the critical point of gain and loss is exceeded [43], which can reimplement TESs and TCSs. It is therefore possible to realize a dual-band topological waveguide, a development which promises to provide a convenient way to achieve flexible wave routing and to transform topological frequencies [44].

In this Letter, a PT-symmetric topological system is constructed by expanding and shrinking unit cells with a diagonally symmetric distribution of gain and loss. Increasing the gain and loss leads to degeneracy and the opening of a bandgap, as the low-frequency TESs and TCSs merge into the bulk states and new TESs and TCSs appear at high frequency. Through theoretical analysis of the Hamiltonian of the non-Hermitian system, the critical points of gain and loss are verified, and a dual-band topological waveguide is realized with appropriate gain and loss.

The non-Hermitian square lattice is composed of diagonally symmetrical gain and loss cylinders, as shown in Fig. 1(a). Cylinder A (gain medium) can be implemented using InGaAsP multiple-quantum wells on the InP substrate, and cylinder B (loss medium) can be implemented by placing thin absorbing Cr/Ge structures on top of the waveguide [45]. The structure is balanced between gain and loss and possesses PT symmetry along the x and y directions. When $d < 0.5a$ ($d > 0.5a$), the intracell distance is less (greater) than the intercell distance, which corresponds to a shrunken (expanded) structure. The expanded and shrunken unit cells are shown in Fig. 1(b).

In a non-Hermitian system, the eigenfrequencies of the band structure vary from all-real values to part-complex values compared to a Hermitian system. When the imaginary part of the relative permittivity γ is small, the gain and loss only slightly affect the real parts of the eigenfrequencies, and the real bands are almost the same for the non-Hermitian system and the corresponding Hermitian system. The topological phases of the system mainly depend on the imaginary parts of the eigenfrequencies [41,42]. When γ increases further, the real bands vary substantially. Comparing Figs. 1(c) and 1(d), it can be seen that as γ increases from 0 to 5, some of the real bands (i.e., the second and third bands, the fourth and fifth bands) become degenerate, and the Dirac point of the fifth and sixth bands is broken, opening up a new photonic band gap (PBG).

The band structure and topological phases of PCs can be approximately calculated through tight binding models. The

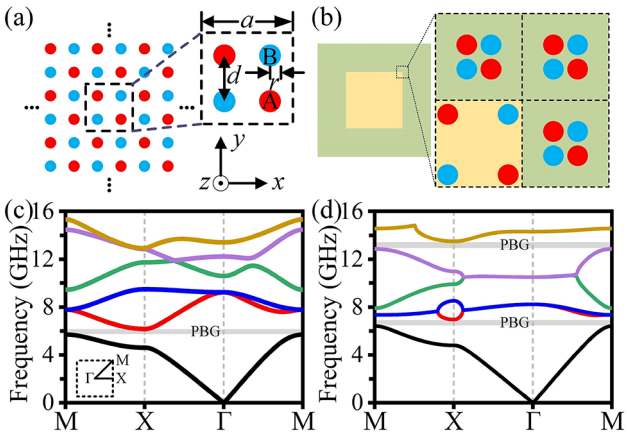

Fig. 1. (a) 2D non-Hermitian PC and its unit cell. The radius of the cylinders is $r = 2.4$ mm; the relative permittivity of cylinders A (gain medium) and B (loss medium) are $\varepsilon_A = \alpha - i\gamma$ and $\varepsilon_B = \alpha + i\gamma$, respectively; the distance between neighboring cylinders is d; and the lattice constant $a = 20$ mm. (b) Schematic of the non-Hermitian topological box-shaped structure; the unit cells are expanded ($d = 0.72a$) in the inner region and shrunken ($d = 0.28a$) in the outer region. (c), (d) Dispersion relation for an expanded unit cell with $\alpha = 6.1$ and with (c) $\gamma = 0$ and (d) $\gamma = 5$.

Hamiltonian of the non-Hermitian system is written as [46]

$$H = \begin{pmatrix} -i\gamma_1 & t_1 + t_2 e^{-ik_x} & t_1 + t_2 e^{-ik_y} & 0 \\ t_1 + t_2 e^{ik_x} & i\gamma_2 & 0 & t_1 + t_2 e^{-ik_y} \\ t_1 + t_2 e^{ik_y} & 0 & i\gamma_3 & t_1 + t_2 e^{-ik_x} \\ 0 & t_1 + t_2 e^{ik_y} & t_1 + t_2 e^{ik_x} & -i\gamma_4 \end{pmatrix}, \quad (1)$$

where t_1 and t_2 represent the intracell and intercell coupling strengths, respectively. Because of the diagonal symmetry of the gain and loss distribution, it can be shown that $-\gamma_1 = \gamma_2 = \gamma_3 = -\gamma_4 = \gamma$.

The transformation matrix is defined as

$$S = \begin{pmatrix} 1 & 0 & 0 & 0 \\ 0 & 0 & 0 & 1 \\ 0 & 0 & 1 & 0 \\ 0 & 1 & 0 & 0 \end{pmatrix}, \quad (2)$$

allowing Eq. (1) to be simplified to a 2×2 block matrix:

$$SHS^{-1} = \begin{pmatrix} -\omega & g \\ g^{\dagger} & \omega \end{pmatrix}, \; g = \begin{pmatrix} A_y e^{-i\theta_y} & A_x e^{-i\theta_x} \\ A_x e^{i\theta_x} & A_y e^{i\theta_y} \end{pmatrix}, \; \omega = \begin{pmatrix} i\gamma & 0 \\ 0 & i\gamma \end{pmatrix}, \quad (3)$$

where $A_j e^{\pm i\theta_j} = t_1 + t_2 e^{\pm ik_j}$, with the subscript j representing the x or y direction. The gain and loss influence the Hamiltonian matrix by altering the diagonal elements from zero to imaginary numbers. The eigenvalues of the Hamiltonian remain unchanged under the similarity transformation and can be calculated through Eq. (3) as $E = \pm\sqrt{(A_x \pm A_y)^2 - \gamma^2}$. This allows the eigenvectors of the first band to be derived as

$$\varphi_1 = \frac{1}{2(E_1 - i\gamma)} \begin{pmatrix} (E_1 - i\gamma)e^{-i\theta_x} \\ A_x + A_y \\ (A_x + A_y)e^{i(\theta_y - \theta_x)} \\ (E_1 - i\gamma)e^{i\theta_y} \end{pmatrix}. \quad (4)$$

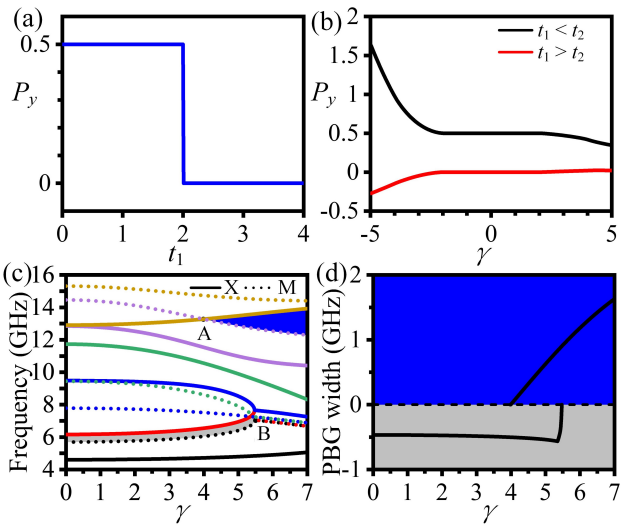

Fig. 2. (a) Variation in polarization P_y with coupling strength t_1 when $t_2 = 2$ and $\gamma = 0$. (b) Variation in polarization P_y with γ when $t_1 = 1$, $t_2 = 2$ or $t_1 = 2$, $t_2 = 1$. (c) Eigenfrequencies of the first six bands at high symmetric points X and M as functions of γ (note: some bands overlap due to degeneracy; for example, on the left side of point B, the second and third bands are degenerate at point M; on the right side of point B, the first and second bands and the third and fourth bands are degenerate at point M, and the second and third bands are degenerate at point X). (d) Variation in PBG width deduced from Fig. 2(c) with γ.

The topological phases are related to 2D polarization through [47]

$$\boldsymbol{P} = \frac{1}{2\pi} \iint \mathrm{d}k_1 \mathrm{d}k_2 \mathrm{Tr}(\boldsymbol{A}_{mn}), \boldsymbol{A}_{mn} = i \langle u_m(\boldsymbol{k}) | \partial_{\boldsymbol{k}} | u_n(\boldsymbol{k}) \rangle, \quad (5)$$

where the integral range is the first Brillouin zone, $u_m(\boldsymbol{k})$ is the Bloch function for the m^{th} band, and the subscripts m, n run over all bands below the PBG.

The polarization can be calculated from Eqs. (4) and (5). It is known that $P_x = P_y$ because of the symmetry of the structure, so we only consider P_y in this Letter. Figures 2(a) and 2(b) show the variation of P_y of the first PBG with coupling strength and non-Hermitian parameters. Figure 2(a) shows that the topological phase transition occurs at $t_1 = t_2$. When $t_1 < 2$, i.e., $t_1 < t_2$ ($t_1 > 2$, i.e., $t_1 > t_2$), $P_y = 0.5$ ($P_y = 0$), the structure possesses a topological non-trivial (trivial) phase. The topological polarization remains invariant in the two respective regions. However, the topological polarization begins to vary when gain and loss are introduced, as shown in Fig. 2(b). The non-Hermitian system has the same polarization as the Hermitian system when $|\gamma| < 2$; when the gain and loss exceed $|\gamma| = 2$, the polarization is no longer a topological invariant.

Tuning the distance of the cylinders in an optical structure is equivalent to tuning the coupling strengths t_1 and t_2 in an electronic system. It is known from previous analysis that the topological phase transition will occur in a photonic system when the distance between cylinders increases from $d = 0.28a$ to $d = 0.72a$, and the PBG will be transformed from a topological trivial phase into a topological non-trivial phase. For a non-Hermitian system, polarization will vary when the gain and loss exceed a critical value, leading to changes in topological properties. It is shown in Fig. 2(c) that the original

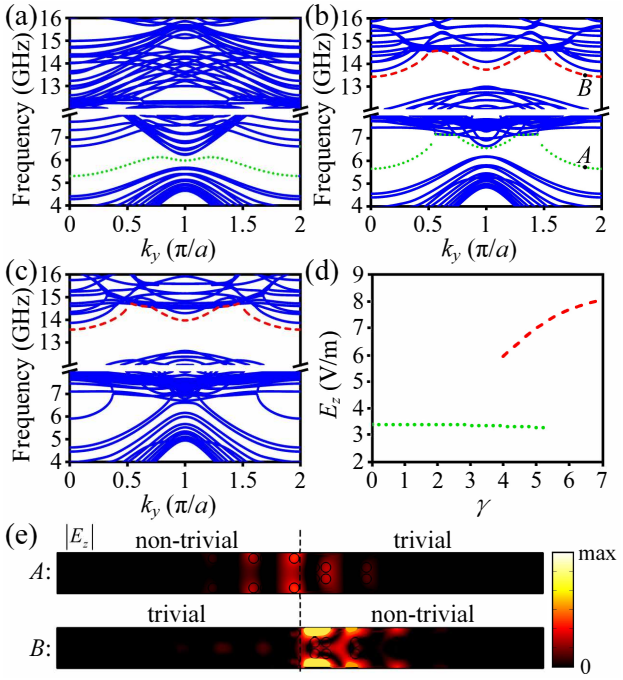

Fig. 3. (a)–(c) Projected bands with $\gamma = 0$, 5, 6, respectively; the frequency ranges from 4 to 8 GHz in the lower region and from 12 to 16 GHz in the top region. The dotted (dashed) line represents low (high) frequency TES bands. (d) Variation in the maximum of the electric field intensity with γ at low frequency (dotted line) and high frequency (dashed line). (e) Eigenmodes of points A and B with $\gamma = 5$.

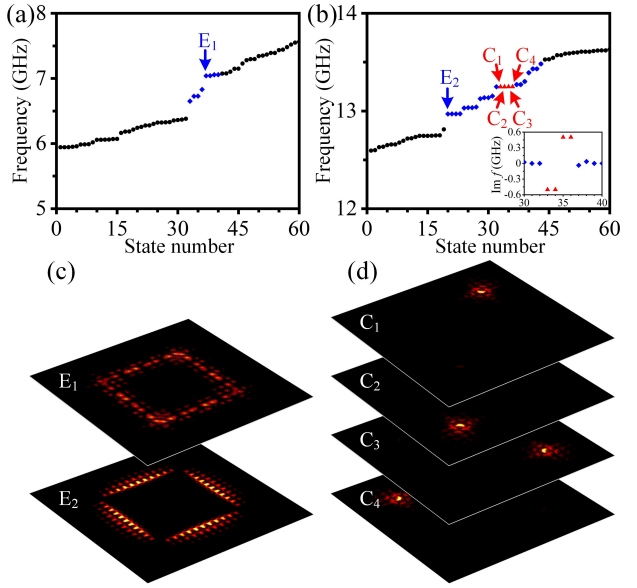

Fig. 4. (a), (b) Real parts of the eigenfrequencies of the non-Hermitian box-shaped structure with $\gamma = 5$; the rhombic (triangular) dots represent TESs (TCSs); (c) TESs for points E_1 and E_2 in Figs. 4(a) and 4(b); (d) TCSs for points C1 to C4 in Fig. 4(b).

low-frequency PBG (light gray area) will degenerate while a new high-frequency PBG (blue/dark gray area) will open up as γ is increased. Furthermore, Fig. 2(d) shows that the low-frequency PBG degenerates at $\gamma = 5.5$ and the high-frequency PBG emerges above $\gamma = 4$. The PBG width is more sensitive to a change in γ at high frequency than at low frequency. The appropriate PBG width and frequency range can be obtained by tuning γ. As TES can only exist in a PBG, these TESs disappear when the topological non-trivial PBG degenerates. Therefore, the quantity and frequency of TES may vary with different gain and loss values.

In order to explore the properties of TESs in non-Hermitian systems, a supercell structure composed of expanded and shrunken unit cells is proposed to visualize the projected bands, as shown in Figs. 3(a)–3(c). The supercell is composed of six expanded unit cells (arranged to the left) and six shrunken unit cells (arranged to the right) extending periodically along the y direction. When $\gamma = 0$, there is a low-frequency topological band with a frequency range of 5.82–6.36 GHz. When γ increases to 5, the frequency range changes to 6.20–6.56 GHz. Simultaneously, due to the new PBG between the fifth and sixth bands, a high-frequency topological band also emerges in the range 13.43–13.68 GHz and dual-band TESs are achieved. As the first PBG degenerates for $\gamma > 5.5$, the low-frequency TESs merge into the bulk state at $\gamma = 6$, and only the high-frequency TESs (13.57–13.86 GHz) remain.

As shown in Fig. 3(d), the electric field intensity of the high-frequency TESs are more sensitive to γ than that of the low frequency TESs. From the eigenmode diagram shown in Fig. 3(e), it is found that at low (high) frequency, the expanded structure possesses a topological non-trivial (trivial) phase, and the shrunken structure possesses a topological trivial (non-trivial) phase. The topological phases of the structure transition as the light shifts from high to low frequency, and the energies of the TESs are both localized mainly in the topological non-trivial structure. By introducing non-Hermiticity, the transition from a low-frequency TES to a high-frequency TES is realized, and a TES with a higher frequency, greater electric field intensity, and better localization is obtained.

In order to prove the topological properties described previously, a box-shaped structure is proposed; the eigenfrequencies and eigenmodes are plotted in Fig. 4. The design of the box-shaped structure is shown in Fig. 1(b): the inner (outer) region is composed of 12×12 expanded (six layers of shrunken) unit cells. It is shown in Fig. 4(c) that by introducing appropriate gain and loss, dual-band TESs can be realized in the box-shaped structure, and the TESs at high frequency have better localization and a greater electric field intensity than that at low frequency. The TCS depends on the polarization of the system [1]:

$$Q_c = 4P_xP_y, \tag{6}$$

where Q_c is a topological invariant related to the TCS. $Q_c = 1$ when $\boldsymbol{P} = (1/2, 1/2)$ and energy is localized at the four corners of the square interface. The Hermitian system possesses TESs and TCSs at low frequency [48]; however, when $\gamma = 5$, there are only TESs at low frequency, as shown in Fig. 4(a). The TCSs disappear as the PBG between the first and second bands narrows; the eigenfrequencies of the low-frequency TCSs are no longer in the PBG, causing the TCSs to merge with the bulk states. Additionally, due to the wide PBG between the fifth and sixth bands, the eigenfrequencies of the TCSs are located in the PBG, and four degenerate TCSs appear at high frequency, as shown in Fig. 4(b). The TCSs of the Hermitian system appear at four vertices of the box-shaped structure at the same time [1,48],

while in the non-Hermitian system, the TCSs are localized at only one corner, as shown in Fig. 4(d). The eigenfrequencies of the four TCSs are two sets of complex conjugate pairs. As seen in Figs. 4(b) and 4(d), the energy is localized in the top-right or bottom-left corner of the box-shaped structure when the imaginary part of the eigenfrequency is negative [corresponding to C_1 and C_2 in Fig. 4(d), respectively]. Meanwhile, when the imaginary part of the eigenfrequency is positive, the energy is localized in the bottom-right or top-left corner of the box-shaped structure [corresponding to C_3 and C_4 in Fig. 4(d), respectively]. Therefore, the positions of the TCSs in the box-shaped structure depend on the sign of the imaginary part of the eigenfrequency.

In summary, we introduced gain and loss into the Hermitian topological system, and by gradually increasing the gain and loss, we found that the TESs and TCSs present at low frequency disappear due to the degeneracy of bands, and that new TESs and TCSs appear at high frequency that have greater energy and better localization. Introducing significant gain and loss can also broaden the PBG and allows the construction of a broadband TES. Our work paves the way to the exploration of intriguing topological properties in non-Hermitian systems with large gain and loss.

Funding. Fundamental Research Funds for the Central Universities (531118040112); Natural Science Foundation of Hunan Province (2017JJ2048, 2020JJ4161); National Natural Science Foundation of China (61405058, 62075059).

Acknowledgment. The authors acknowledge Prof. J. Liu for software sponsorship.

Disclosures. The authors declare no conflicts of interest.

Data availability. Data underlying the results presented in this Letter are not publicly available at this time but may be obtained from the authors upon reasonable request.

REFERENCES

1. B. Xie, H. Wang, H. Wang, X. Zhu, J. Jiang, M. Lu, and Y. Chen, Phys. Rev. B **98**, 205147 (2018).
2. B. Yan, J. Xie, E. Liu, Y. Peng, R. Ge, J. Liu, and S. Wen, Phys. Rev. Appl. **12**, 044004 (2019).
3. M. L. N. Chen, L. Jiang, Z. Lan, and W. E. I. Sha, IEEE Trans. Antennas Propag. **68**, 609 (2020).
4. Y. Peng, B. Yan, J. Xie, E. Liu, H. Li, R. Ge, F. Gao, and J. Liu, Phys. Status Solidi RRL **14**, 2000202 (2020).
5. X. Zhou, J. Wu, and Y. Wu, Opt. Commun. **466**, 125653 (2020).
6. C. Lu, C. Wang, M. Xiao, Z. Zhang, and C. Chan, Phys. Rev. Lett. **126**, 113902 (2021).
7. A. Shi, B. Yan, R. Ge, J. Xie, Y. Peng, H. Li, W. E. I. Sha, and J. Liu, Opt. Lett. **46**, 1089 (2021).
8. E. Nussbaum, E. Sauer, and S. Hughes, Opt. Lett. **46**, 1732 (2021).
9. W. Ruan, X. He, F. Zhao, and J. Dong, J. Lightwave Technol. **39**, 889 (2021).
10. Y. Wei, B. Yan, Y. Peng, A. Shi, D. Zhao, R. Peng, Y. Xiang, and J. Liu, Opt. Lett. **46**, 3941 (2021).
11. X. Zhang, H. Wang, Z. Lin, Y. Tian, B. Xie, M. Lu, Y. Chen, and J. Jiang, Nat. Phys. **15**, 582 (2019).
12. R. E. Christiansen, F. Wang, and O. Sigmund, Phys. Rev. Lett. **122**, 234502 (2019).
13. X. Ni, K. Chen, M. Weiner, D. J. Apigo, C. Prodan, A. Alù, E. Prodan, and A. B. Khanikaev, Commun. Phys. **2**, 55 (2019).
14. W. A. Benalcazar, B. A. Bernevig, and T. L. Hughes, Science **357**, 61 (2017).
15. Z. N. Farzad and R. Fleury, Phys. Rev. Lett. **123**, 053902 (2019).
16. H. Huang and F. Liu, Phys. Rev. B **100**, 085119 (2019).
17. J. Wang, Y. Yang, N. Dai, and Y. Xu, Phys. Rev. Lett. **126**, 206404 (2021).
18. C. M. Bender and S. Boettcher, Phys. Rev. Lett. **80**, 5243 (1998).
19. B. Zhen, C. Hsu, Y. Igarashi, L. Lu, I. Kaminer, A. Pick, S. Chua, J. D. Joannopoulos, and M. Soljačić, Nature **525**, 354 (2015).
20. S. K. Özdemir, S. Rotter, F. Nori, and L. Yang, Nat. Mater. **18**, 783 (2019).
21. S. Longhi, J. Phys. A: Math. Theor. **44**, 485302 (2011).
22. Z. Lin, H. Ramezani, T. Eichelkraut, T. Kottos, H. Cao, and D. N. Christodoulides, Phys. Rev. Lett. **106**, 213901 (2011).
23. L. Feng, Y. Xu, W. S. Fegadolli, M. Lu, J. E. B. Oliveira, V. R. Almeida, Y. Chen, and A. Scherer, Nat. Mater. **12**, 108 (2013).
24. H. Yin, R. Bai, X. Gu, C. Zhang, G. Gu, Y. Zhang, X. Jin, and Y. P. Lee, Opt. Commun. **414**, 172 (2018).
25. K. G. Makris, R. El-Ganainy, D. N. Christodoulides, and Z. H. Musslimani, Phys. Rev. Lett. **100**, 103904 (2008).
26. D. V. Novitsky, A. Karabchevsky, A. V. Lavrinenko, A. S. Shalin, and A. V. Novitsky, Phys. Rev. B **98**, 125102 (2018).
27. S. Longhi, Phys. Rev. A **82**, 031801 (2010).
28. Y. Sun, W. Tan, H. Li, J. Li, and H. Chen, Phys. Rev. Lett. **112**, 143903 (2014).
29. B. Midya, H. Zhao, and L. Feng, Nat. Commun. **9**, 2674 (2018).
30. Y. Xiong, J. Phys. Commun. **2**, 035043 (2018).
31. L. Jin and Z. Song, Phys. Rev. B **99**, 081103 (2019).
32. S. Longhi, Phys. Rev. Res. **1**, 023013 (2019).
33. W. Zhu, W. Teo, L. Li, and J. Gong, Phys. Rev. B **103**, 195414 (2021).
34. S. Yao, F. Song, and Z. Wang, Phys. Rev. Lett. **121**, 136802 (2018).
35. S. Yao and Z. Wang, Phys. Rev. Lett. **121**, 086803 (2018).
36. H. Shen, B. Zhen, and L. Fu, Phys. Rev. Lett. **120**, 146402 (2018).
37. A. Ghatak and T. Das, J. Phys.: Condens. Matter **31**, 263001 (2019).
38. J. Claes and T. L. Hughes, Phys. Rev. B **103**, L140201 (2021).
39. H. Zhao, X. Qiao, T. Wu, B. Midya, S. Longhi, and L. Feng, Science **365**, 1163 (2019).
40. B. Midya, Ann. Phys. **421**, 168280 (2020).
41. M. Wang, L. Ye, J. Christensen, and Z. Liu, Phys. Rev. Lett. **120**, 246601 (2018).
42. Z. Zhang, M. R. López, Y. Cheng, X. Liu, and J. Christensen, Phys. Rev. Lett. **122**, 195501 (2019).
43. S. Zhang and L. Jin, Phys. Rev. A **100**, 043808 (2019).
44. K. K. Om and K. H. Kim, Phys. Status Solidi RRL **16**, 2100427 (2021).
45. Z. Wong, Y. Xu, J. Kim, K. O. Brien, Y. Wang, L. Feng, and X. Zhang, Nat. Photonics **10**, 796 (2016).
46. C. Yuce and H. Ramezani, Phys. Rev. A **100**, 032102 (2019).
47. F. Liu and K. Wakabayashi, Phys. Rev. Lett. **118**, 076803 (2017).
48. B. Xie, G. Su, H. Wang, H. Su, X. Shen, P. Zhan, M. Lu, Z. Wang, and Y. Chen, Phys. Rev. Lett. **122**, 233903 (2019).